2023 IEEE International Conference on Robotics and Automation (ICRA 2023)
May 29 - June 2, 2023. London, UK

Development and Experimental Verification of a 3D Dynamic Absolute Nodal Coordinate Formulation Model of Flexible Prostate Biopsy/Brachytherapy Needles

Athanasios Martsopoulos[1,2,3], Thomas L. Hill[1],
Rajendra Persad[4], Stefanos Bolomytis[4] and Antonia Tzemanaki[1,2]

***Abstract*— Robot-assisted percutaneous needle insertion is expected to significantly increase targeting accuracy in minimally invasive operations. For this, it is necessary to provide mathematical models that can accurately capture the underlying dynamics of medical needles. Here, we present a novel nonlinear mathematical model of flexible medical needles based on the Absolute Nodal Coordinate Formulation. The model allows the description of large needle deflections and arbitrarily large rigid body motions. Tailored to the requirements of transperineal prostate biopsy and brachytherapy, it can correlate both the translational and rotational coordinates of the needle's base with its deflection, provide force feedback and accept arbitrary loading conditions. The model is optimised in terms of computational efficiency in order to allow real-time simulation and control. Experiments show that the proposed model allows for submillimeter precision in both static and dynamic needle deflection settings. Due to its accuracy and computational efficiency, it is expected to constitute a valuable tool for both real-time visual/haptic simulation and control of percutaneous needle insertion.**

I. INTRODUCTION

Minimally invasive surgery (MIS) and localised therapy are integral parts of modern medical practices, as they offer decreased recovery time, reduced patient discomfort and lower risk of infection, when compared to open surgery [1]. Percutaneous needle insertion is one of the main MIS methods, including a plethora of diagnostic and therapeutic applications, such as prostate biopsy/brachytherapy, illustrated in Fig. 1, neurosurgery, and deep brain stimulation [2]. Alongside its advantages, accurate percutaneous needle placement carries significant challenges. The limited visual feedback during the operation, combined with factors, such as tissue anisotropy, heterogeneity and variability in anatomical structures among different patients, complicates navigation through the tissue and thus decreases the operation's overall accuracy [3]. This can lead to imprecise targeting, which, in turn, can cause severe complications, such as false negatives in biopsy or ablation of healthy tissue [1]. Robot-assisted needle insertion offers the potential to increase the accuracy of such procedures and, as a result, has been at the forefront of recent studies.

[1] School of Civil, Aerospace and Mechanical Engineering, University of Bristol, UK {athanasios.martsopoulos, antonia.tzemanaki, tom.hill}@bristol.ac.uk
[2] Bristol Robotics Laboratory, UK
[3] University of the West of England, Bristol, UK
[4] Bristol Urological Institute, Southmead Hospital, Bristol, UK

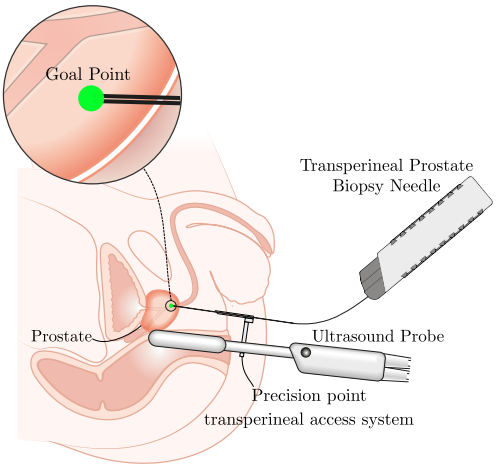

Fig. 1. Illustration of transperineal prostate biopsy/brachytherapy procedure adapted from [5].

A prerequisite for implementing this robotic solution is the formulation of mathematical models that can accurately capture the dynamics of needle insertion. In most cases, this modelling is divided into three main parts [4]: a) the modelling of the soft tissue, b) the characterisation of the interaction forces between the needle and the surrounding medium (Fig. 2) and c) the modelling of the flexible needle. This division allows the development of decoupled mathematical models for the needle and the tissue, while needle-tissue interaction is often modelled based on experimentally derived generalised force profiles at the needle's base during needle insertion procedures [1]. Our work focuses on the formulation of models of flexible medical needles, the importance of which is analysed in the following sections.

A. Related work

Complete mathematical models of flexible medical needles aim to provide both visual and haptic information with regards to the system's state [2]. As a result, such models have to identify the relationship between the spatio-temporal behaviour of the needle's geometry and the specified motion trajectory at its base (e.g. insertion velocity, axial and lateral rotation), under the effect of some arbitrary loading conditions acting on its shaft. Furthermore, the models aim to provide information about the reaction forces at the needle's base, due to the combined effect of the input driving

constraints and the input loading conditions [2].

In [6], the non-holonomic kinematic model of flexible medical needles that was proposed, constituted the starting point for a plethora of kinematics-based needle models and motion planning algorithms, e.g. [7] and [8]. While kinematic models are characterised by high computational efficiency, their various assumptions lead to low accuracy [9]. More specifically, they fail to model the interaction between the needle and the surrounding tissue, and, hence, cannot provide information about the dynamics of needle insertion or provide haptic feedback.

The need for more accurate needle models and information about the dynamic properties of needle insertion has led to a transition from kinematic to mechanics-based modelling approaches. [10]–[12] presented quasi-static needle models, based on the linear Euler-Bernoulli beam theory, that described needle deflection during percutaneous insertion procedures. While this modelling approach offers simplicity and computational efficiency, its linearity assumption leads to invalid solutions when large deflections are considered [13], [14]. Furthermore, linear approaches cannot describe arbitrarily large rigid body motions, as linear strain theory is invariant to finite rigid body rotations, leading to non-volume preserving solutions and visual artefacts for the flexible body [15]. To account for the geometric nonlinearity and minimise the targeting error of linear modelling approaches, [16] and [14] use quasi-static methods based on the nonlinear 2D and 3D Finite Element Method (FEM). Similarly, [17] presents a geometrically nonlinear quasi-static model of flexible needles based on FEM and the co-rotational formulation. These models provide both computational efficiency and high accuracy when compared to experimental results for describing the steady-state responses of both large and small needle deflections.

Both linear and nonlinear models, described above, estimate needle deflection assuming a quasi-static needle insertion. This assumes that the needle is inserted at a rate that does not allow for any oscillatory transients to occur, and deflection is approximated by a sequence of steady-state responses. This assumption, however, does not provide any information about the vibrational behaviour of the needle and does not account for the correlation between its deflection and the system's input parameters, such as its insertion velocity and the rate of axial rotation. Specifically, [12], [18]–[21] have proven the strong coupling of parameters such as the needle insertion speed, vibration and axial rotation to the needle-tissue interaction forces and, subsequently, to its deflection. Furthermore, axial needle rotation and vibration can be used for minimising needle deflection during needle insertion procedures [12], [22]–[24]. Incorporation of such parameters requires a dynamic model of flexible needles and not a quasi-static one. Therefore, accounting for the underlying needle dynamics is crucial for the complete characterisation of needle insertion and, subsequently, for the development of robust robot control algorithms [25].

In this regard, [9] presented a novel dynamic model of a rigid/flexible 2D needle. The model was based on the Rayleigh-Ritz approximation technique and the linear Euler-Bernoulli beam theory. This work was one of the first to introduce the importance of dynamic modelling in needle insertion procedures but did not account for geometric nonlinearities as it was based on a linear beam model. In [26], we employed both the Rayleigh-Ritz and the FEM approaches for capturing the three-dimensional dynamics of a rigid/flexible model of brachytherapy needles. However, the proposed models were based on infinitesimal strain theory and thus, did not account for geometric nonlinearities and large needle deflections. Similarly, [25] extended the static angular spring FEM approach of [14]: the model captured the dynamics of needle insertion while accounting for geometric nonlinearities due to large deflection, but it was only limited to 2D applications.

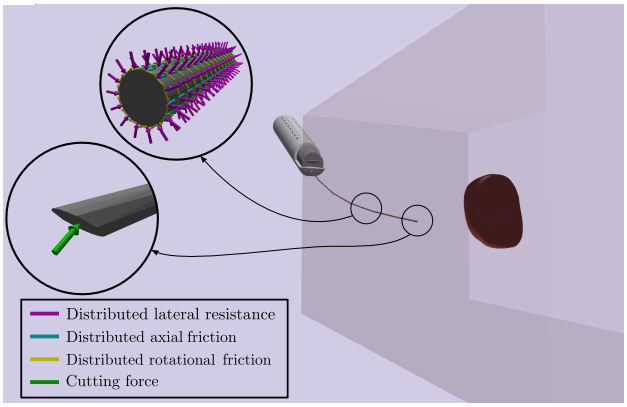

Fig. 2. Illustration of post-puncture needle-tissue interaction forces.

B. Contributions

Extending the work of [9], [25] and [26], this paper develops a novel modelling approach that aims to provide a complete characterisation of the three-dimensional dynamics of flexible medical needles. The proposed model is based on the absolute nodal coordinate formulation (ANCF) proposed in [27]. The method allows the description of arbitrarily large rigid-body displacements/rotations, geometric nonlinearities and large deformations of flexible bodies, as well as a straightforward addition of complex force functions and constraint equations [28]. These features makes it a perfect candidate for the requirements of transperineal prostate biopsy/brachytherapy, illustrated in Fig. 1, in which the surgeon's hand performs large rigid body motions to guide the needle in the desired goal point and retrieve a sample for analysis or for providing localised treatment. Furthermore, it utilises a specially designed beam element, introduced in [27], which allows high numerical efficiency and alleviation of numerical problems (e.g. element/shear locking) for the case of thin and long structures, such as the thin flexible needles studied in our work.

The accuracy and computational efficiency of the model is verified experimentally. To the best of the authors' knowledge, this is the first work to investigate and employ the theory of ANCF for modelling the dynamics of flexible med-

ical needles. It is also the first to investigate both large rigid body motion of the needle's base and large needle deflections, experimentally evaluate needle dynamics, investigate aspects of computational efficiency and relax the modelling assumptions of previous works in the literature (e.g. linearity assumptions, unmodelled dynamics, 2D models).

The paper is organised as follows: Section II presents the formulation of the proposed needle model, including discussions on solution strategies and computational efficiency in II-D. Section III describes the experimental design and the associated experimental studies for the verification of the proposed needle model. Concluding remarks and future extensions are given in Section IV.

II. METHODS

A. Problem formulation

As shown in Fig. 3, the proposed multibody model consists of two connected bodies: a rigid base, that can follow any arbitrary trajectory imposed by the surgeon's hand, and the flexible needle, which is attached to the rigid base and deflects under the effect of a general 3D force field resulting from its interaction with the surrounding tissue, Fig. 2. To describe the motion of the system, we introduce the following frames of reference: let F be the inertial frame of reference and f_c a frame rigidly attached to the rigid base centre of mass C. Furthermore, we introduce the frame f which is rigidly attached to point A of the rigid base and which constitutes the reference for the description of the needle's displacement field. As shown in Fig. 3, the orientation of frames f_c and f is identical and remains fixed. The ANCF method employs a spatial discretisation of the needle's geometry into n_e beam elements, each of which is described using inertially measured nodal coordinates. More specifically, as shown in Fig. 3, a complete characterisation of the configuration of the beam element $j \in [1, n_e]$ can be acquired based on the inertially measured cross-sectional position and orientation at its nodes A_j and B_j, while intermediate points are defined with the help of interpolation functions. The element's vector of generalised coordinates can be defined as

$$\underline{e}_j = \underline{e}_j(t) = \left[\underline{r}_{A_j}^T, \underline{r}_{x_{A_j}}^T, \underline{r}_{B_j}^T, \underline{r}_{x_{B_j}}^T\right]^T, \tag{1}$$

with

$$\begin{aligned} \underline{r}_{A_j} &= \underline{r}^F_{OA_j/F}, \quad \underline{r}_{x_{A_j}} = \frac{\partial \underline{r}^F_{OA_j/F}}{\partial x_j}, \\ \underline{r}_{B_j} &= \underline{r}^F_{OB_j/F}, \quad \underline{r}_{x_{B_j}} = \frac{\partial \underline{r}^F_{OB_j/F}}{\partial x_j}. \end{aligned} \tag{2}$$

The inertial position of point P_j of element j, illustrated in Fig. 3, can be obtained with the help of the generalised element coordinates and the interpolation function matrix $\boldsymbol{S}(x_j)$ as

$$\underline{r}^F_{OP_j/F}(x_j, t) = \underline{r}_j(x_j, t) = \boldsymbol{S}(x_j)\ \underline{e}_j. \tag{3}$$

The interpolation function matrix can be defined as

$$\boldsymbol{S}(x_j) = [S_1(x_j)\boldsymbol{I}_3,\ S_2(x_j)\boldsymbol{I}_3,\ S_3(x_j)\boldsymbol{I}_3,\ S_4(x_j)\boldsymbol{I}_3]$$

with

$$\begin{aligned} S_1 &= \frac{1}{2} - \frac{3}{4}\xi_j + \frac{\xi_j^3}{4}, \quad S_2 = \frac{l_j}{8}\left(1 - \xi_j - \xi_j^2 + \xi_j^3\right), \\ S_3 &= \frac{1}{2} + \frac{3}{4}\xi_j - \frac{\xi_j^3}{4}, \quad S_4 = \frac{l_j}{8}\left(-1 - \xi_j + \xi_j^2 + \xi_j^3\right), \end{aligned} \tag{4}$$

$\boldsymbol{I}_3$ being the 3×3 identity matrix and $\xi_j = 2(x_j/l_j) - 1$. In equation (3), x_j is the local longitudinal coordinate of element j, illustrated in Fig. 3b, while l_j is its initial length. The spatial derivatives of the inertial position of point P_j are defined as as

$$\underline{r}_{x_j} = \frac{\partial \underline{r}_j}{\partial x_j} = \frac{d\boldsymbol{S}(x_j)}{dx_j}\ \underline{e}_j = \boldsymbol{S}_x(x_j)\ \underline{e}_j$$

and

$$\underline{r}_{xx_j} = \frac{\partial^2 \underline{r}_j}{\partial x_j^2} = \frac{d^2\boldsymbol{S}(x_j)}{dx_j^2}\ \underline{e}_j = \boldsymbol{S}_{xx}(x_j)\ \underline{e}_j.$$

B. Virtual work

The virtual work of the inertial forces of element j can be defined as

$$\delta W_j^{(in)} = \int_{m_j} (\ddot{\underline{r}}^F_{OP_j/F})^T \delta \underline{r}^F_{OP_j/F}\ \mathrm{d}m_j. \tag{5}$$

Using equation (3) we can prove that

$$\delta W_j^{(in)} = \ddot{\underline{e}}_j^T \boldsymbol{M}_j^T \delta \underline{e}_j, \tag{6}$$

with

$$\boldsymbol{M}_j = \rho_j A_j \int_0^{l_j} \boldsymbol{S}^T(x_j)\boldsymbol{S}(x_j)\mathrm{d}x_j. \tag{7}$$

The quantity ρ_j represents the density of the beam element, while A_j is its cross-sectional area. Note that the mass matrix is constant.

To define the virtual work of the elastic forces, we employ the elastic line approach introduced in [27]. The virtual work of the elastic forces results from the combined effect of axial and bending deformations [27]. The axial strain component ϵ_j can be obtained with the help of the Green-Lagrange deformation gradient, while the curvature κ_j of the element's

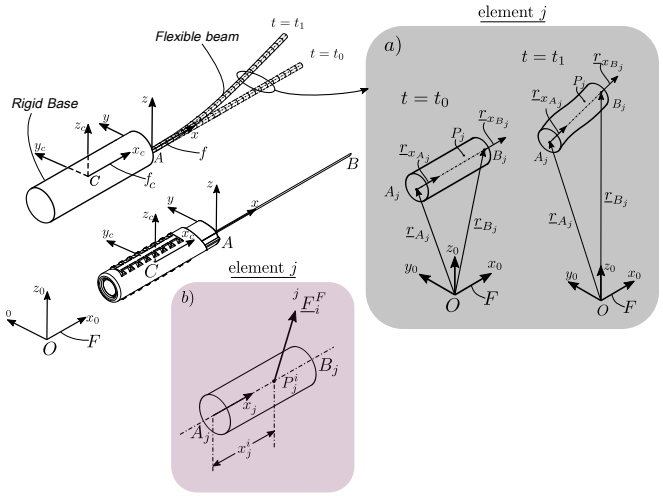

Fig. 3. Needle model and the three-dimensional ANCF element. a) Presents the element j at it's reference and deformed state. b) Presents the free body diagram of the element j.

centerline can be defined based on the Frenet–Serret frame formulation [27]. These can be expressed as

$$\epsilon_j = \frac{1}{2}(\underline{r}_{x_j}^T \underline{r}_{x_j} - 1) \quad \text{and} \quad \kappa_j = \frac{\|\underline{r}_{x_j} \times \underline{r}_{xx_j}\|}{\|\underline{r}_{x_j}\|^3}. \tag{8}$$

We also assume that the second moments of area with respect to y and z axes are equal, that is $I_j = I_{y_j} = I_{z_j}$. Based on (8), the element's total elastic energy Π_j can be defined as

$$\Pi_j^{(el)} = \frac{1}{2}\int_0^{l_j} E_j A_j \epsilon_j^2 + E_j I_j \kappa_j^2 \mathrm{d}x_j, \tag{9}$$

with E_j the element's Young modulus. Then, the variation of the elastic energy is given as

$$\delta W_j^{(el)} = -\left(\frac{\partial \Pi_j^{(el)}}{\partial \underline{e}_j}\right)^T \delta \underline{e}_j. \tag{10}$$

Combining equations (8), (9) and (10) it can be proved that the virtual work of the elastic forces can be written as

$$\delta W_j^{(el)} = \underline{Q}_{el_j}^T \delta \underline{e}_j, \quad \text{with} \quad \underline{Q}_{el_j} = \underline{Q}_{a_j} + \underline{Q}_{b_j} \tag{11}$$

where

$$\underline{Q}_{a_j} = -\int_0^{l_j} E_j A_j \epsilon_j \left(\frac{\partial \epsilon_j}{\partial \underline{e}_j}\right)^T \mathrm{d}x_j \tag{12}$$

and

$$\underline{Q}_{b_j} = -\int_0^{l_j} E_j I_j \kappa_j \left(\frac{\partial \kappa_j}{\partial \underline{e}_j}\right)^T \mathrm{d}x_j. \tag{13}$$

Next, we define the virtual work for the external forces. For this, it is assumed that a random point P_j^i of element j, located at the beam's elastic line and at a distance $0 < x_j^i < l_j$ from the nodal point A_j, is subjected to a point force ${}^j\underline{F}_i^F(t, \underline{e}_j, \dot{\underline{e}}_j)$ shown in Fig. 3b. Then, the virtual work resulting from this force is

$$\delta W_j^{(ex)} = ({}^j\underline{F}_i^F)^T \delta \underline{r}^F_{OP_j^i/F} = ({}^j\underline{F}_i^F)^T \boldsymbol{S}(x_j^i)\delta \underline{e}_j. \tag{14}$$

The virtual work of the external generalised forces presented in equation (14) can be extended to accommodate for n_f point forces. In this case, it can be proven that the total virtual work of the external generalised forces is given as

$$\delta W_j^{(ex)} = \underline{Q}_{f_j}^T \delta \underline{e}_j, \quad \text{with} \quad \underline{Q}_{f_j} = \sum_{i=1}^{n_f} \boldsymbol{S}^T(x_j^i)({}^j\underline{F}_i^F). \tag{15}$$

To formulate the system's constraint and damping forces we first introduce the mapping from the local generalised coordinates $\underline{e}_j$ of element j to the flexible beam global generalised coordinates $\underline{q}$, such that $\underline{e}_j = \boldsymbol{L}_j \underline{q}$. Based on the global coordinates, the virtual work of the global external generalised constraint forces for element j can be calculated as $\delta W^{(c)} = \underline{Q}_c^T \delta \underline{q}$. Damping forces can be calculated as

$$\delta W^{(d)} = \underline{Q}_d^T \delta \underline{q}, \quad \text{with} \quad \underline{Q}_d^T = -\boldsymbol{C}\dot{\underline{q}}.$$

The global damping matrix $\boldsymbol{C}$ can be calculated using techniques, such as the Caughey or the Rayleigh damping [29], and tuned based on experimental data. Finally, integrals in (12), (13) and (7) can be computed numerically with the help of Gaussian quadrature. As suggested in [27], the axial strain components in equation (12) can be approximated with five integration points, while three integration points are sufficient for the bending integral in equation (13).

C. Equations of motion

To derive the flexible needle's equations of motion, we apply the dynamic equilibrium expression based on D'Alembert's form of the principle of virtual work, which can be written as

$$\delta W^{(in)} = \delta W^{(el)} + \delta W^{(d)} + \delta W^{(ex)} + \delta W^{(c)}.$$

The virtual works of the above expression can be calculated considering the contributions from the individual elements as

$$\sum_{j=1}^{n_e} \delta W_j^{(in)} = \sum_{j=1}^{n_e} \left(\delta W_j^{(el)} + \delta W_j^{(ex)}\right) + \delta W^{(d)} + \delta W^{(c)}.$$

Substituting the derived virtual work expressions, the above equation becomes

$$\sum_{j=1}^{n_e} \left(\boldsymbol{M}_j \ddot{\underline{e}}_j - \underline{Q}_{el_j} - \underline{Q}_{f_j}\right)^T \delta \underline{e}_j - \left(\underline{Q}_{d_j} + \underline{Q}_{c_j}\right)^T \delta \underline{q} = 0.$$

Based on the mapping between the global and local coordinates $\underline{e}_j = \boldsymbol{L}_j \underline{q}$, the above expression can be written as

$$(\boldsymbol{M}\ddot{\underline{q}} - \underline{Q}_{el} - \underline{Q}_d - \underline{Q}_f - \underline{Q}_c)^T \delta \underline{q} = 0, \tag{16}$$

with

$$\boldsymbol{M} = \sum_{j=1}^{n_e} \boldsymbol{L}_j^T \boldsymbol{M}_j \boldsymbol{L}_j, \quad \underline{Q}_f = \left(\sum_{j=1}^{n_e} \boldsymbol{L}_j^T \underline{Q}_{f_j}\right) + \underline{Q}_P,$$

and

$$\underline{Q}_{el} = \sum_{j=1}^{n_e} \boldsymbol{L}_j^T \underline{Q}_{el_j}.$$

In the expression above, the vector $\underline{Q}_P$ corresponds to the point loads applied at the system's nodal coordinates. Due to the explicit integration of the constraint forces $\underline{Q}_c$, the generalised coordinates of the flexible body can be treated as independent and, thus, its equations of motion can be expressed as

$$\boldsymbol{M}\ \ddot{\underline{q}} = \underline{Q}_{el} + \underline{Q}_d + \underline{Q}_f + \underline{Q}_c. \tag{17}$$

D. Solution strategy

The state vector $\underline{q}$ in equation (17) contains the boundary conditions, due to the rigid connection between the flexible needle and the rigid base. To eliminate the boundary conditions, the state vector $\underline{q}$ can be partitioned in the constrained $\underline{q}_c \in \mathbb{R}^{n_c}$ and active $\underline{q}_a \in \mathbb{R}^{n_a}$ coordinates such that $\underline{q} = \left[\underline{q}_c^T, \underline{q}_a^T\right]^T$. The constrained vector $\underline{q}_c$ incorporates the prescribed motion of the associated coordinates (boundary conditions), while the active (or free) vector $\underline{q}_a$ describes the free (independent) coordinates that define the beam's motion. Based on the above partitioning and equation (17), the system's equations of motion can be rewritten as

$$\begin{bmatrix} \boldsymbol{M}_{cc} & \boldsymbol{M}_{ca} \\ \boldsymbol{M}_{ac} & \boldsymbol{M}_{aa} \end{bmatrix} \begin{bmatrix} \ddot{\underline{q}}_c \\ \ddot{\underline{q}}_a \end{bmatrix} = \begin{bmatrix} \underline{g}_c(t, \underline{q}, \dot{\underline{q}}) \\ \underline{g}_a(t, \underline{q}, \dot{\underline{q}}) \end{bmatrix}, \tag{18}$$

where

$$\begin{bmatrix} \underline{g}_c(t, \underline{q}, \dot{\underline{q}}) \\ \underline{g}_a(t, \underline{q}, \dot{\underline{q}}) \end{bmatrix} = \begin{bmatrix} \underline{Q}_{el_c} \\ \underline{Q}_{el_a} \end{bmatrix} + \begin{bmatrix} \underline{Q}_{d_c} \\ \underline{Q}_{d_a} \end{bmatrix} + \begin{bmatrix} \underline{Q}_{f_c} \\ \underline{Q}_{f_a} \end{bmatrix} + \begin{bmatrix} \underline{Q}_{c_c} \\ \underline{Q}_{c_a} \end{bmatrix}.$$

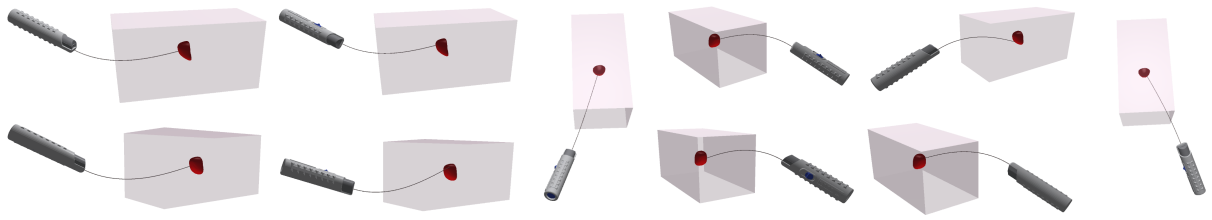

Fig. 4. Visualisation of the proposed ANCF method for modelling a transperineal prostate biopsy/brachytherapy needle. The method can model accurately and in real-time the dynamics of the needle for arbitrarily large rigid body motions and flexible deformations.

Note, that $\underline{Q}_{c_a} = \underline{0}_{n_a}$ as there are no constraint forces associated with the free coordinates of the system. Based on this observation, equation (18) can be written as

$$\underline{\ddot{q}}_a = \boldsymbol{M}_{aa}^{-1} \left(\underline{Q}_{el_a} + \underline{Q}_{d_a} + \underline{Q}_{f_a} - \boldsymbol{M}_{ac}\, \underline{\ddot{q}}_c \right). \qquad (19)$$

Equation (19) can be integrated numerically to obtain the temporal evolution of the active coordinates $\underline{q}_a$. Haptic feedback can be obtained using the forces acting on the needle's support (point A shown in Fig. 3). These can be calculated with the help of (18) as

$$\underline{Q}_{c_c} = \boldsymbol{M}_{cc}\underline{\ddot{q}}_c + \boldsymbol{M}_{ca}\underline{\ddot{q}}_a - \underline{Q}_{el_c} - \underline{Q}_{d_c} - \underline{Q}_{f_c}. \qquad (20)$$

Equations (19) and (20) can be used for obtaining the needle's state under arbitrary driving constraints, such as the desired translational and rotational velocity of its base and arbitrary loading conditions, due to the needle's interactions with the surrounding tissue, illustrated in Fig. 2. The distributed forces can be added to the needle model as generalised external loads with the help of equations (15). Using the technique of *surface embedding* [30], the ANCF mesh can be bound to a high-resolution surface mesh for high fidelity results. This is illustrated in Fig. 4, in which the computational needle mesh was bound to a virtual transperineal prostate biopsy/brachytherapy needle. The model allows the real-time visualisation of the needle for arbitrary rigid body motions, needle deflections and loading conditions.

III. EXPERIMENTS

A. Experimental design

For the verification of the proposed computational needle model, we have developed the experimental setup of Fig. 5. It is comprised of the Schunk Lwa4p robotic arm equipped with a specially designed end-effector, in which a flexible transperineal prostate biopsy needle with $0.27\mathrm{m}$ length is rigidly attached. Furthermore, the setup includes two global shutter high frame rate cameras (Daheng Imaging MER-160, 220 FPS) for capturing the needle's deflection and vibration. The synchronisation of the tracking and robotic systems as well as their communication is achieved using the Robotic Operating System (ROS). The user interface, shown in Fig. 6, was also designed in OpenGL for controlling the robotic arm and visualising the system's state.

The needle's state is estimated with the help of image processing and photogrammetry. More specifically, first

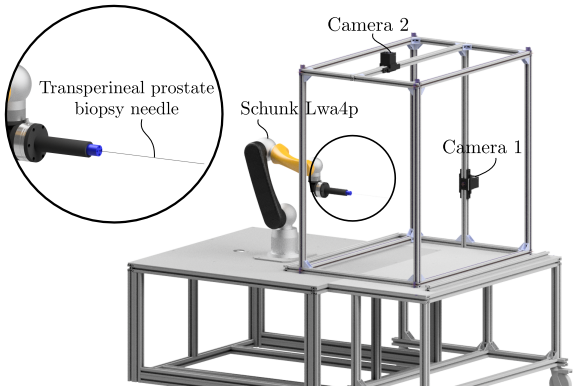

Fig. 5. Experimental setup.

the images from the two cameras, shown in Fig. 6, are transformed into binary and their background is extracted. Next, using principles from photogrammetry and projective geometry, the corresponding points between the two images are found and are used for constructing an estimate of the three-dimensional needle's state. This is defined by the position, velocity and acceleration of the point cloud depicted with green points in Fig. 6. The estimated point cloud is then animated in real-time in the virtual environment, as shown in Fig. 6.

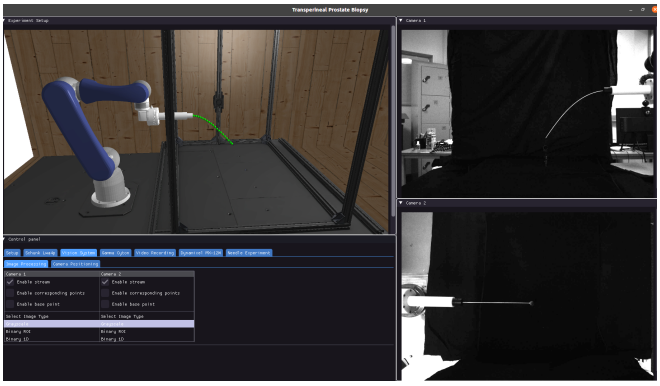

Fig. 6. User interface for controlling the experimental setup.

Simulations were implemented on a 8-core Intel(R) Core(TM) i7-9700 CPU running at 3.0GHz, using the C++ Armadillo library [31] with the Intel Math Kernel Library (MKL) integration. Aspects of algorithmic parallelisation

were implemented using the OpenMP API [32]. To tackle numerical stiffness and to allow large time steps and real-time simulation, numerical integration of equation (19) was implemented with the help of implicit numerical solvers. To accelerate computations, the Jacobian $\frac{\partial \underline{Q}_{el}}{\partial \underline{q}_a}$ of the elastic forces $\underline{Q}_{el}$ was analytically calculated by differentiating expressions (12) and (13). The proposed model allowed for highly-efficient real-time simulations with integration frequencies of more than 100 Hz.

For the following experiments, the flexible needle was modelled as a homogeneous stainless steel beam with a circular cross-section of radius $r = 0.635\text{mm}$ and length of $L = 0.27\text{m}$. Both its mechanical and geometrical properties were assumed to remain constant along its span. All physical parameters were based on commercially available bevelled tip prostate biopsy needles, as the one illustrated in Fig. 1.

As discussed in Section I, due to tissue properties such as its anisotropy and heterogeneity, needle-tissue interaction forces have a stochastic nature and cannot be known with certainty prior to the operation. Thus, the proposed needle deformation model was tested using a wide range of *known* loads, driving constraints and boundary conditions applied along the needle's geometry. These were chosen with ranges close to the ones expected for the needle to experience during a transperineal prostate biopsy/brachytherapy. More specifically, two sets of experiments were conducted. In the first set, the needle's base was kept fixed, while its tip

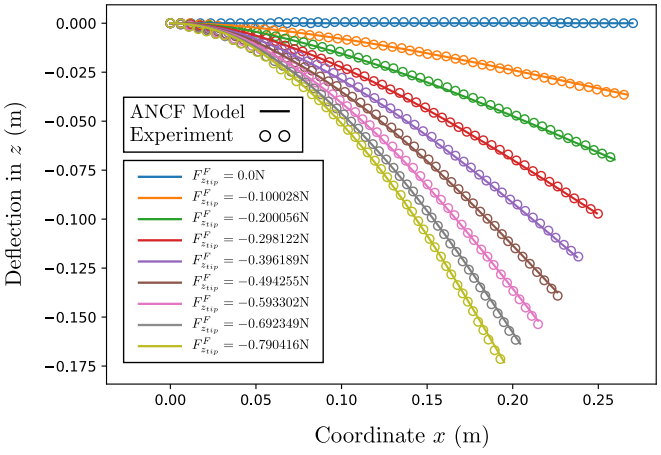

Fig. 7. Needle tip loading with incremental weights. Variability among experiments was negligible and thus no statistical metrics are reported.

was loaded with incrementally increasing weights ranging from 0 to 80 grams. The needle deflection with respect to its local frame f and the exact tip loading conditions, are illustrated in Fig. 7. In the second set of experiments, part of the needle's distal geometry, including the tip, was kept fixed with the help of a clamping device, while its base was allowed to rotate. A sinusoidal pitch (around the local y axis) rotation of 10^o range and 0.2Hz frequency was chosen to simulate driving inputs during the operation. This loading is similar to the one presented in Fig. 1, where part of the needle's geometry is laterally constrained due to its

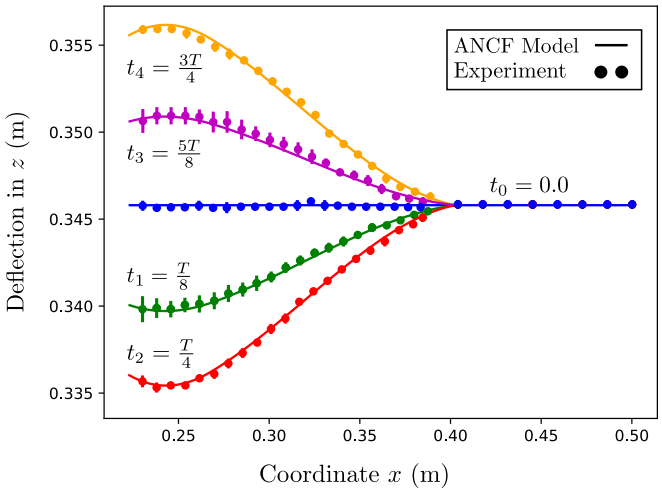

Fig. 8. Dynamic needle experiment with part of the needle fixed and its base moving. The figure illustrates the needle deflection in different time instances, with $T = 5$s. The data points denote the experiments average, while error bars denote standard deviation. Sample size is $n = 10$.

interaction with the tissue, while its base is still performing rigid body motion. In this experiment, 40% of the needle's distal length was kept fixed while the rest was allowed to move freely. Results in various time instances are presented in Fig. 8. As illustrated in Fig. 7 and 8, the proposed model leads to highly accurate deflection profiles, even for large needle deformations, in both static and dynamic settings. More specifically, the root mean squared error between the experimental observations and the model in the static experiments of Fig. 7 was 0.63mm, while for the dynamic experiments of Fig. 8 was 0.431mm. The maximum standard deviation observed in the experimental data of Fig. 8 was 0.75mm. Both results satisfy the application's requirements as the current average targeting error for manual prostate biopsy and brachytherapy procedures is over 5.5mm [33].

IV. CONCLUSION AND FUTURE WORK

This work presented a novel mathematical model for capturing the three-dimensional dynamics of flexible medical needles. The model, which was tailored to the requirements of transperineal prostate biopsy/brachytherapy, allowed for an accurate and computationally efficient solution. The accuracy of the proposed model was verified experimentally, exceeding the requirements for the targeted application. It should be noted that the reported results solely refer to the needle deflection and do not include the deformations of the surrounding tissue. However, the presented approach can be easily integrated with soft tissue dynamics to provide a holistic needle insertion simulator. Future work will use this model and the presented experimental infrastructure for the development of such a system.

ACKNOWLEDGMENT

This work was supported by EPSRC under Grant EP/S021795/1. For the purpose of open access, the authors have applied a Creative Commons Attribution (CC BY) license to any Accepted Manuscript version arising.

REFERENCES

[1] A. M. Okamura, C. Simone, and M. D. O'Leary, "Force modeling for needle insertion into soft tissue," *IEEE Transactions on Biomedical Engineering*, vol. 51, no. 10, pp. 1707–1716, Oct. 2004.

[2] G. Ravali and M. Muniyandi, "Haptic Feedback in Needle Insertion Modeling and Simulation: Review," *IEEE Reviews in Biomedical Engineering*, vol. PP, 2017.

[3] N. Abolhassani, R. Patel, and M. Moallem, "Needle insertion into soft tissue: A survey," *Medical engineering & physics*, vol. 29, pp. 413–31, 2007.

[4] O. Goksel, S. Salcudean, and S. Dimaio, "3D simulation of needle-tissue interaction with application to prostate brachytherapy," *Computer aided surgery : official journal of the International Society for Computer Aided Surgery*, vol. 11, pp. 279–88, 2006.

[5] Cancer Research UK, "Diagram showing a transperineal prostate biopsy CRUK," 2016, Licensing CC BY-SA 4.0. [Online]. Available: {https://commons.wikimedia.org/wiki/File:Diagram_showing_a_transperineal_prostate_biopsy_CRUK_473.svg}

[6] I. Robert J. Webster, J. S. Kim, N. J. Cowan, G. S. Chirikjian, and A. M. Okamura, "Nonholonomic Modeling of Needle Steering," *The International Journal of Robotics Research*, vol. 25, no. 5-6, pp. 509–525, 2006.

[7] B. Fallahi, M. Khadem, C. Rossa, R. Sloboda, N. Usmani, and M. Tavakoli, "Extended bicycle model for needle steering in soft tissue," in *2015 IEEE/RSJ International Conference on Intelligent Robots and Systems (IROS)*, Sep. 2015, pp. 4375–4380.

[8] G. J. Vrooijink, M. Abayazid, S. Patil, R. Alterovitz, and S. Misra, "Needle path planning and steering in a three-dimensional non-static environment using two-dimensional ultrasound images," *The International Journal of Robotics Research*, vol. 33, pp. 1361–1374, 9 2014.

[9] M. Khadem, C. Rossa, N. Usmani, R. S. Sloboda, and M. Tavakoli, "A Two-Body Rigid/Flexible Model of Needle Steering Dynamics in Soft Tissue," *IEEE/ASME Transactions on Mechatronics*, vol. 21, no. 5, pp. 2352–2364, Oct. 2016.

[10] A. Asadian, M. R. Kermani, and R. V. Patel, "An analytical model for deflection of flexible needles during needle insertion," in *2011 IEEE/RSJ International Conference on Intelligent Robots and Systems*, Sep. 2011, pp. 2551–2556, iSSN: 2153-0858.

[11] T. Lehmann, C. Rossa, N. Usmani, R. S. Sloboda, and M. Tavakoli, "A Real-Time Estimator for Needle Deflection During Insertion Into Soft Tissue Based on Adaptive Modeling of Needle–Tissue Interactions," *IEEE/ASME Transactions on Mechatronics*, vol. 21, no. 6, pp. 2601–2612, Dec. 2016.

[12] N. Abolhassani, R. V. Patel, and F. Ayazi, "Minimization of needle deflection in robot-assisted percutaneous therapy," *The International Journal of Medical Robotics and Computer Assisted Surgery*, vol. 3, no. 2, pp. 140–148, 2007.

[13] K. E. Bisshopp and D. C. Drucker, "Large deflection of cantilever beams," *Quarterly of Applied Mathematics*, vol. 3, no. 3, pp. 272–275, 1945, publisher: Brown University.

[14] O. Goksel, E. Dehghan, and S. E. Salcudean, "Modeling and simulation of flexible needles," *Medical Engineering & Physics*, vol. 31, no. 9, pp. 1069 – 1078, 2009.

[15] M. Müller and M. H. Gross, "Interactive virtual materials," in *Graphics Interface*, 2004.

[16] S. P. DiMaio and S. E. Salcudean, "Interactive simulation of needle insertion models," *IEEE Transactions on Biomedical Engineering*, vol. 52, no. 7, pp. 1167–1179, Jul. 2005.

[17] Y. Adagolodjo, L. Goffin, M. De Mathelin, and H. Courtecuisse, "Robotic insertion of flexible needle in deformable structures using inverse finite-element simulation," *IEEE Transactions on Robotics*, vol. 35, no. 3, pp. 697–708, 6 2019.

[18] L. Tan, X. Qin, Q. Zhang, H. Zhang, H. Dong, T. Guo, and G. Liu, "Effect of vibration frequency on biopsy needle insertion force," *Medical Engineering & Physics*, vol. 43, pp. 71 – 76, 2017.

[19] C. McGill, J. Schwartz, J. Moore, P. McLaughlin, and A. Shih, "Effects of insertion speed and trocar stiffness on the accuracy of needle position for brachytherapy," *Medical physics*, vol. 39, pp. 1811–7, 2012.

[20] M. Abayazid, M. Kemp, and S. Misra, "3D flexible needle steering in soft-tissue phantoms using Fiber Bragg Grating sensors," in *2013 IEEE International Conference on Robotics and Automation*, May 2013, pp. 5843–5849, iSSN: 1050-4729.

[21] N. Abolhassani, R. Patel, and F. Ayazi, "Effects of Different Insertion Methods on Reducing Needle Deflection," in *2007 29th Annual International Conference of the IEEE Engineering in Medicine and Biology Society*, Aug. 2007, pp. 491–494, iSSN: 1558-4615.

[22] R. Tsumura, Y. Takishita, and H. Iwata, "Needle insertion control method for minimizing both deflection and tissue damage," vol. 4, no. 1, 3 2019.

[23] N. A. Wood, K. Shahrour, M. C. Ost, and C. N. Riviere, "Needle steering system using duty-cycled rotation for percutaneous kidney access," in *2010 Annual International Conference of the IEEE Engineering in Medicine and Biology*, 8 2010, pp. 5432–5435.

[24] S. Badaan, D. Petrisor, C. Kim, P. Mozer, D. Mazilu, L. Gruionu, A. Patriciu, K. Cleary, and D. Stoianovici, "Does needle rotation improve lesion targeting?" vol. 7, no. 2, pp. 138–147, 6 2011.

[25] A. Haddadi and K. Hashtrudi-Zaad, "Development of a dynamic model for bevel-tip flexible needle insertion into soft tissues," *Conference proceedings : ... Annual International Conference of the IEEE Engineering in Medicine and Biology Society. IEEE Engineering in Medicine and Biology Society. Conference*, vol. 2011, pp. 7478–82, 2011.

[26] A. Martsopoulos, Persad Rajendra, Bolomytis Stefanos, Hill Thomas L., and Tzamanaki Antonia, "Spatial rigid/flexible dynamic model of biopsy and brachytherapy needles under a general force field," in *2020 IEEE International Conference on Intelligent Robots and Systems (IROS)*, Oct. 2020.

[27] J. Gerstmayr and A. A. Shabana, "Analysis of Thin Beams and Cables Using the Absolute Nodal Co-ordinate Formulation," *Nonlinear Dynamics*, vol. 45, no. 1, pp. 109–130, Jul. 2006.

[28] A. A. Shabana, "Flexible multibody dynamics: Review of past and recent developments," *Journal of Multibody System Dynamics*, pp. 189–222, 1997.

[29] J. Humar, *Dynamics of Structures: Second Edition*. Taylor & Francis, 2002.

[30] "Accurate surface embedding for higher order finite elements," in *Proceedings of the 12th ACM SIGGRAPH/Eurographics Symposium on Computer Animation - SCA '13*. ACM Press, p. 187.

[31] C. Sanderson and R. Curtin, "Armadillo: a template-based c++ library for linear algebra," *Journal of Open Source Software*, vol. 1, no. 2, p. 26, 2016.

[32] L. Dagum and R. Menon, "Openmp: An industry-standard api for shared-memory programming," *IEEE Comput. Sci. Eng.*, vol. 5, no. 1, p. 46–55, Jan. 1998.

[33] M. Khadem, C. Rossa, R. S. Sloboda, N. Usmani, and M. Tavakoli, "Ultrasound-guided model predictive control of needle steering in biological tissue," vol. 01, no. 1, 2016.